JLMN-Journal of Laser Micro/Nanoengineering Vol. 20, No. 3, 2025

Modification of Femtosecond Laser Absorption by Electron Beam Irradiation

Nicolai Schneider[*1,2], **Lova Chechik**[1,2], **Michael Schmidt**[1,2], **and Kristian Cvecek**[1,2]
[1]*Institute of Photonic Technologies, Friedrich-Alexander-University Erlangen-Nuremberg, Erlangen, Germany*
[2]*Erlangen Graduate School in Advanced Optical Technologies (SAOT), Friedrich-Alexander-University Erlangen-Nuremberg, Erlangen, Germany*
[*]*Corresponding author's e-mail: nicolai.schneider@lpt.uni-erlangen.de*

Dielectric materials interact with ultra-fast lasers through various nonlinear absorption mechanisms, leading to ionization of the material. Specifically, quasi-free electrons are generated in the conduction band via multiphoton ionization (MPI) or tunneling ionization. When the density of these quasi-free electrons exceeds a critical threshold, ablation of the material occurs. In this work, the influence of extrinsically seeded electrons on the laser ablation threshold and the crater morphology on soda-lime glass for femtosecond laser single-shot experiments is investigated. For this, the laser was focused inside a modified scanning electron microscope, where the soda-lime glass samples were installed. Results show that irradiation with extrinsic electrons, provided by the SEM electron gun, can increase the ablation volume and decrease the ablation threshold.

DOI: 10.2961/jlmn.2025.03.2004
Keywords: femtosecond laser, ablation threshold, electron irradiation, surface structuring, glass, crater analysis

1. Introduction

Since the development of the first pulsed lasers in 1960 by Maiman [1] and the first continuous-wave laser a year later by Javan et al. [2], lasers have been implemented in industrial processing and scientific research across nearly all material types and states of matter. The first picosecond ($<10^{-9}$ s) lasers, developed almost a decade later have been proven to have a significant scientific and technological impact on a variety of topics, including controlled thermonuclear research, time measurements at the order of the pulse duration, and more [3]. Finally, the emergence of the first femtosecond (10^{-15} s) lasers in the early 1980s by Fork et al. [4] enabled local processing of thermally sensitive transparent materials like glasses and polymers in the micro- and nanometer range, without modifying or damaging the surrounding areas outside the desired ablation zone [5].

For materials with quasi-free electrons, e.g. metals, and using near-IR radiation, the energy transfer between the laser and the material is mainly governed by electrons directly absorbing the laser photons (linear absorption). However, defect-free high bandgap dielectrics like fused silica (E_{gap} ~9 eV) appear transparent to the same radiation, since the valence electrons can only absorb photons with energies exceeding the bandgap energy, i.e. UV-radiation. At sufficiently high intensities, achievable by pulsed lasers, absorption of energy by non-linear absorption processes like multiphoton absorption is possible [6], where a single electron absorbs multiple photons at once, thus surpassing the bandgap. The ablation threshold, defined as the minimum intensity or fluence needed for dielectrics to absorb laser radiation and ablate, is determined by the material's band gap energy, among other factors. For average fluences above the ablation threshold, the ablation area and thus the ablation resolution is governed by the laser's minimum spot size, fundamentally restricted by the diffraction limit.

In this work, high energy electrons (4.5 keV) are injected into the material by an electron beam, thereby generating localized distributions of free (ionized) and quasi-free (conduction band) electrons on their trajectory. While the trajectory is dictated by the electron beam properties and the material. For example, a 1 keV beam on fused silica leads to a distribution smaller than 30x30x30 nm³ [7]. These (quasi-)free electrons should allow absorption of sub-threshold intensity laser radiation, effectively lowering the ablation threshold within the extents of the free electron distribution.

2. Materials and methods

2.1 Experimental Setup

The laser used in this work was an 800 nm femtosecond laser (Coherent Astrella USP-1K, see Table 1) with a $1/e^2$ beam diameter of ~13mm. The laser employs a chirped pulse amplification and thus the pulse duration can be changed by adapting the distance between the gratings via a motor, effectively allowing to impose an up- or downchirp onto the pulse. The pulse duration was measured with an autocorrelator (Pulse Scout UPG-LR – Newport Corp.). The experimental setup is shown in Fig. 1. Since the laser does not support intrinsic power control and the pulse energy of 7.5mJ is several magnitudes above the expected energies required for ablation, it was attenuated via a two-stage system.In the first stage, attenuation is achieved via a zero-order half-wave plate and a UVFS Thin Film Brewster type polarizer, enabling precise power control. In the second stage, a wedged plate is used to extract the first reflection (~ 8 %) for the experiment, while the transmitted and the second reflection are directed into a beam dump. The scanning electron microscope (SEM) used is a Philips/FEI XL30 with a tungsten

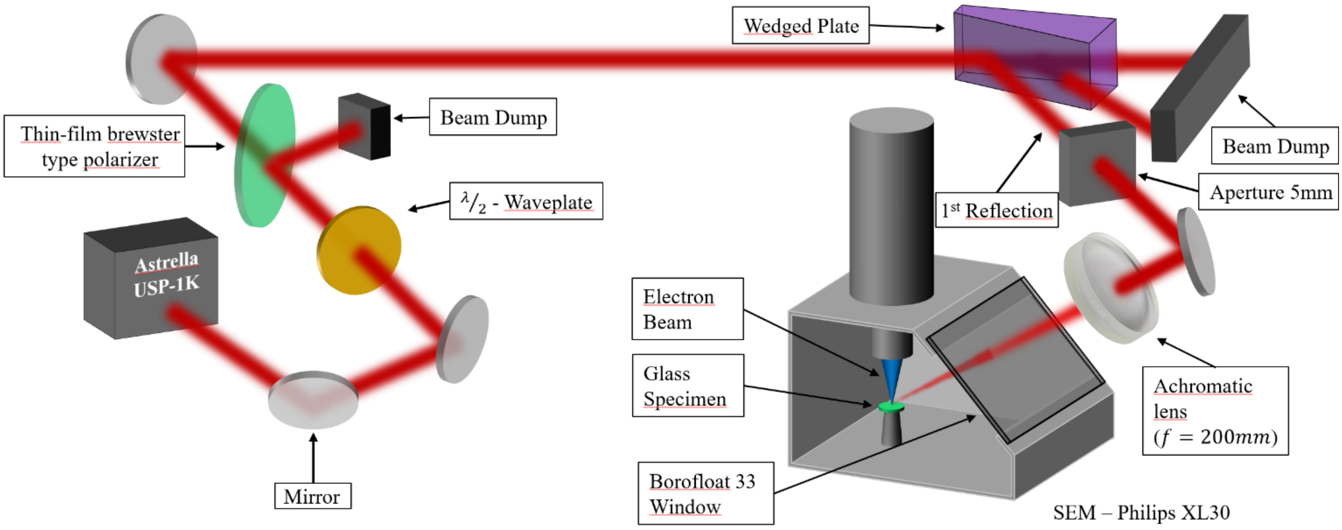

Fig. 1 Experimental setup for electron manipulated femtosecond laser absorption on glass. The laser is attenuated via a two-stage system, consisting of a thin-film brewster type polarizer and a zero-order half waveplate, followed by a fused silica wedged plate. The scanning electron microscope (XL30-Tungsten) is retrofitted with a Borofloat© 33 glass panel.

cathode, retrofitted with a Borofloat© 33 glass panel on the backside. In order to minimize the chromatic aberration due to the laser bandwidth of ~ 30 nm FHWM it is focused into the SEM with an achromatic lens (f = 200 mm).

Table 1 Coherent Astrella USP-1K specifications

Specification	Value
Repetition Rate (kHz)	1
Pulse Energy (mJ)	7.5
Min. Pulse Duration (fs)	35
Center Wavelength (nm)	800
Beam diameter ($1/e^2$) (mm)	13
Polarization state	linear
M^2X	1.2
M^2Y	1.1

All ablation experiments are carried out under vaccuum conditions at a pressure of $7.5 - 8.5 * 10^{-8}$ bar. The “TV-Mode” of the SEM moves the beam line for line over the scan field with a vertical repetition frequency of ~60 Hz and horizontal frequency in the kHz range.

The material used for the ablation experiments are soda-lime glass microscope slides. Prior to the experiments the glass slides are cleaned in an ultrasonic bath in ethanol for ten minutes, rinsed with isopropyl alcohol and dried in warm air for 15 minutes. The glass samples are attached to an aluminum SEM stub using carbon tabs without any kind of metallic coating.

2.2 Ablation experiments

As a reference value the ablation threshold for single pulse irradiation was determined according to Liu [8] without any prior electron injection. Assuming a $sech^2$ pulse, the pulse duration was 160 fs. The sample is positioned beyond the focal plane, resulting in a larger spot diameter. Four different pulse energies were applied: 87.6 µJ, 101.9 µJ, 128.9 µJ and 157.0 µJ. In order to investigate the influence of electron irradiation on the absorption and thus the crater morphology and the ablation threshold, the laser single-shot experiments with varying pulse energies were repeated, but preceded by electron irradiation for three seconds. For electron irradiation, the SEM was operated in TV scan mode at a magnification of 800×, corresponding to an irradiated area of 150 µm × 84 µm, with a working distance of 11.3 mm. The acceleration voltage was set to 4.5 kV and the software-based spot size to three. The scanning surface was irradiated with the electron beam until the SE detector signal no longer changed and consequently the charging effect of the electrically insulating glass reached an equilibrium state. An exposure time of approximately three second to the electron beam was sufficient to achieve this state. To ensure that any changes in the laser-material interactions were caused exclusively by the electrons, the laser setup and, consequently, the laser incidence conditions were left unchanged between the two experimental series.

2.3 Ablation crater analysis

The analyses and measurements of the ablation craters were carried out by with a confocal laser scanning microscope (LSM; LEXT OLS4000, OLYMPUS) with a laser wavelength of 405 nm. All crater images were taken with each crater centered in the field of view with frame integration of four images. The glass slides were cleaned in an ultrasonic bath in ethanol for ten minutes, rinsed with isopropyl alcohol and dried in warm air for 15 minutes.

To correct any leveling misalignment of the specimens, the images were surface tilt corrected. A 50× apochromatic objective lens in addition with 2x digital zoom was chosen. For each crater, 90 radial profiles were extracted at 2° angular intervals from the center of the fitted ellipse. The environmental surface level close to the crater was

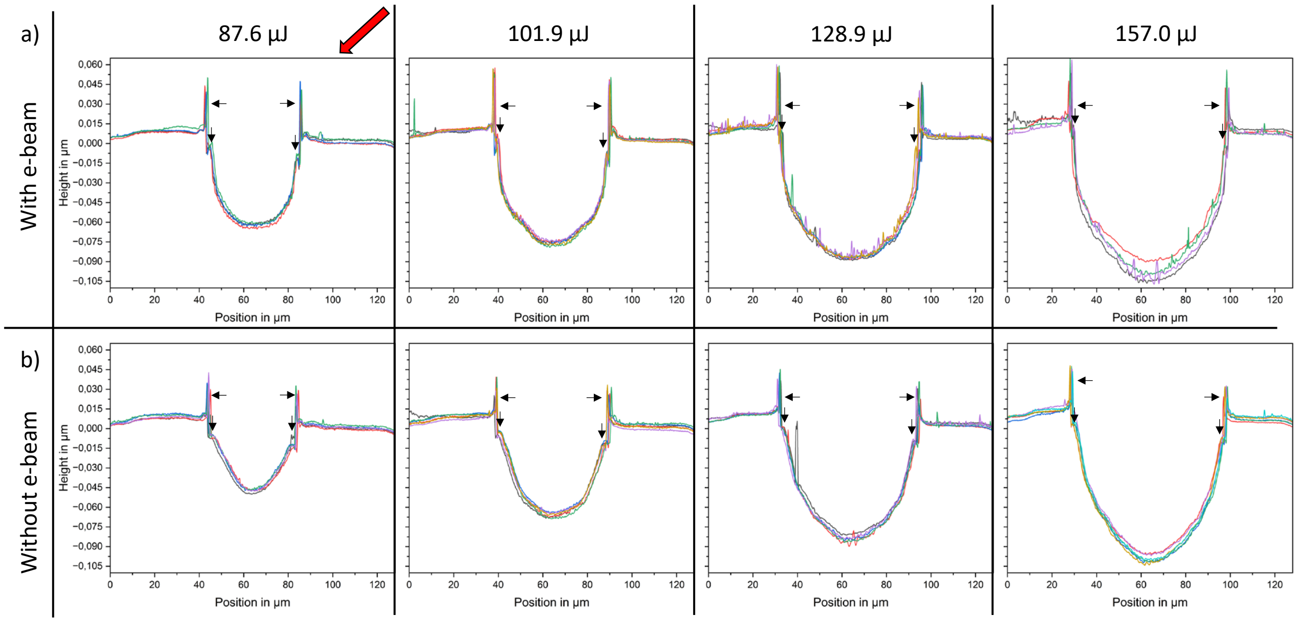

Fig. 3 Horizontal height profiles of the ablation craters for the different pulse energies. a) Experiments with electron beam irradiation. b) Experiments without electron irradiation. The incidence direction of the laser is marked by the red arrow. Primary and secondary rings are marked by horizontal and vertical arrows, respectively.

extrapolated across the crater to give a baseline. The first intersection between the height profile, starting from the crater center, and the environmental level was defined as the crater boundary. An ellipse was fitted to the datapoints with the software Python using the direct least squares approach described in Halíř & Flusser [9] enabling the calculation of the crater volume and area (see Fig. 2).

For the volume evaluation, all datapoints within the fitted ellipses, E, were isolated. Since the fitted ellipse was defined as the crater boundary at the environmental zero level, it is also defining a zero-level plane, which was subtracted from all datapoints. The height, $z(x,y)$, was subsequently integrated over the area of the ellipse, A, to calculate the crater volume V:

$$A = \iint_E dx\,dy\,, \tag{1}$$

$$V = \left| \iint_E z(x,y)\; dx\,dy \right|. \tag{2}$$

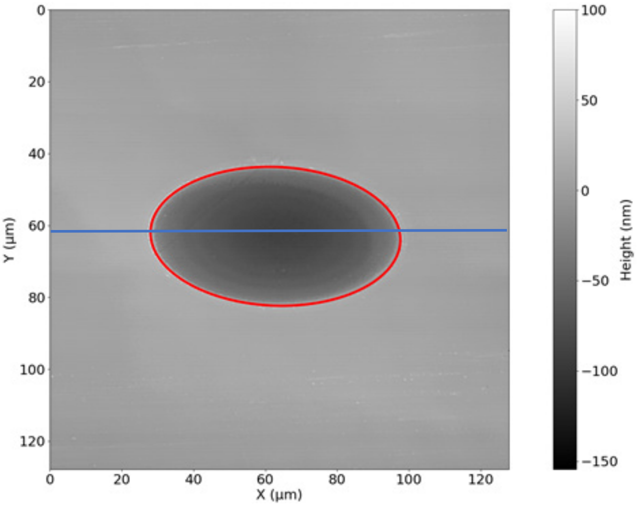

Fig. 2 Example ellipse fit on an ablation crater. The area of the fitted ellipse (red line) can be directly derived and defines the ablation area. The horizontal height profile was taken along the blue line (see Fig. 3).

3. Results and Discussion

Horizontal height profiles (Fig. 2, blue line) in the center of each crater were extracted (Fig. 3). The laser incidence vector is marked by the red arrow. The profile analysis outside the irradiated area showed a variability of 15-20nm in height, as the glass sample is not perfectly flat in itself, explaining the height variability from left to right.

Around the ablation craters, defined by the ellipses, a rim is observable. The heights of the primary outer crater rims (Fig. 3, horizontal arrows) are unaffected by a variation of the pulse energies in the results presented in accordance with the literature [10]. With the preceding electron beam irradiation (Fig. 3a), the rim height is significantly higher compared to the non-irradiated specimens. Ben-Yakar et al. derived, that the build-up of primary rings is due to a thin surface layer which is molten by electron-phonon coupling of the ionization formed plasma. The plasma pressure, resulting in a radial pressure gradient drives the molten material outwards. Due to rapid heat conduction cooling, the accumulated melt layer solidifies outside resulting in the elevated rim surrounding the ablation crater [11]. According to their work, the rim height, ε, is proportional to:

$$\varepsilon \propto \frac{\langle p_{pl} \rangle \langle h_m \rangle^2}{\mu L^2}, \tag{3}$$

with the average plasma pressure $\langle p_{pl} \rangle$, the average melt layer thickness $\langle h_m \rangle$, the melt viscosity μ and the crater radius L. Comparing the rim heights (see Fig. 3) electron irradiation increases ε by roughly 50% while simultaneously increasing the crater size. Assuming that the electron beam delivers more free electrons prior to the incoming pulse, the absorption coefficient should rise significantly, leading to a higher plasma density and hence also $\langle p_{pl} \rangle$. In addition, more absorbed energy would result in a higher melt temperature, with μ falling exponentially with temperature [12].

Secondary rims within the crater (Fig. 3, vertical arrows) are a product of swift atomization at the center of the irradiated area where the fluence is the highest, creating a crater within a crater [13].

The ablation threshold E_{th} was investigated based on a modified approach of Liu [8] where the squared crater diameter, D^2, can be expressed by:

$$D^2 = 2w_0^2 \ln\left(\frac{F}{F_{th}}\right) = 2w_0^2 \ln\left(\frac{E}{E_{th}}\right), \tag{4}$$

with the fluence F, the threshold fluence F_{th}, the spot size w_0, the pulse energy, E, and threshold pulse energy, E_{th}, respectively [14]. Since the laser in the experiments presented here is incident at an angle resulting in an elliptical spot and crater, it is not possible to determine a single crater diameter. With $D^2 = 4\ A / \pi$, equation (4) can then be solved for the crater area A:

$$A(E) = \frac{A_0}{2} \ln\left(\frac{E}{E_{th,A}}\right), \tag{5}$$

with A_0 being the spot area on the surface.

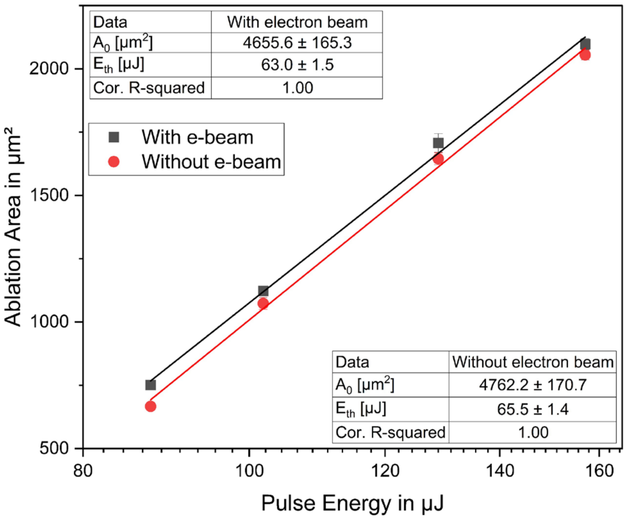

Fig. 4 Ablation crater area plotted against the pulse energy without (red circles) and with (black squares) prior electron beam irradiation. The data was fitted using equation (5). E_{th} is the derived threshold energy, defined by the intersection of the fit-function and the x-axis.

By plotting A against the pulse energy in a semi-logarithmic plot, a straight line is obtained accordingly (see Fig. 4).

Fitting equation (5) to the data points resulted in a corrected R^2 of 0.996. The data points were nonlinearly fitted with the software Origin (OriginLab Corp.) utilizing the Levenberg Marquardt algorithm and a Chi-squared tolerance value of 10^{-9}. Within the scope of the error, the slopes of both straight lines and thus the spot area of both test series are the same, yielding an irradiation area of 4656 µm^2 with and 4762 µm^2 without electron beam irradiation, respectively. As deduced from the profile sections, the crater areas of the irradiated samples also larger than those of the non-irradiated samples. In terms of the fit function, this can be attributed to a lower ablation threshold value E_{th}. The materials initial threshold energy was fitted to 65.5 µJ, with the electron beam irradiation decreasing it by 3.79 % to 63.0 µJ. Since A_0 describes the actual laser irradiated area on the specimen surface the threshold fluences can be estimated via $F_{0,th} = 2E_{th,A}/A_0$ to ~2.76 J cm^{-2} for the initial state and ~2.70 J cm^{-2} after electron irradiation [15]. It is important to note that the Liu model and thus the derivation of the real w_0^2 and A_0, respectively, accounts solely for an ideal gaussian beam profile. Since a hard aperture considerably truncates the beam in the experiments presented (5mm aperture, 13mm beam diameter), the profile on the sample surface resembles an Airy profile rather than a Gaussian profile. The flatter intensity gradient of the Airy profile within its central lobe results in a larger cross-sectional area of material positioned in proximity to the ablation threshold. Consequently, incremental increases in peak fluence yield a more pronounced expansion of the ablated zone for Airy profiles compared to Gaussian profiles. This phenomenon can be attributed to the enhanced threshold sensitivity arising from the greater volume of material in the vicinity of the threshold. As a result, the Liu equation fit and its modification should overestimate the beam radius w_0 (or spot area, A_0), which in turn leads to an apparent underestimation of the threshold fluence. Thus, the absolute values should not be compared quantitatively with the literature values, generated at vertical incidence and with Gaussian beam profiles. Nevertheless, the thresholds can be used to deduce the impact of electron irradiation on the material under the same experimental parameters, if the laser setup remains unchanged as in this work.

For the volume evaluation another modification to equation (5) was done. According to Ben-Yakar et al., the maximum depth of an ablation crater h, in combination with the fluence to energy adaption, can be estimated by [16]:

$$h(E) = \delta_{eff} * \ln\left(\frac{E}{E_{th}}\right), \tag{6}$$

where δ is the effective penetration depth. Approximating the crater shape by a paraboloid [17], the volume is defined by $V = ½ * h * A_0$ thus equation (5) and (6) can be combined to [18]:

$$V(E) = \frac{A_0 \delta_{eff}}{4} * \left[\ln\left(\frac{E}{E_{th,V}}\right)\right]^2. \tag{7}$$

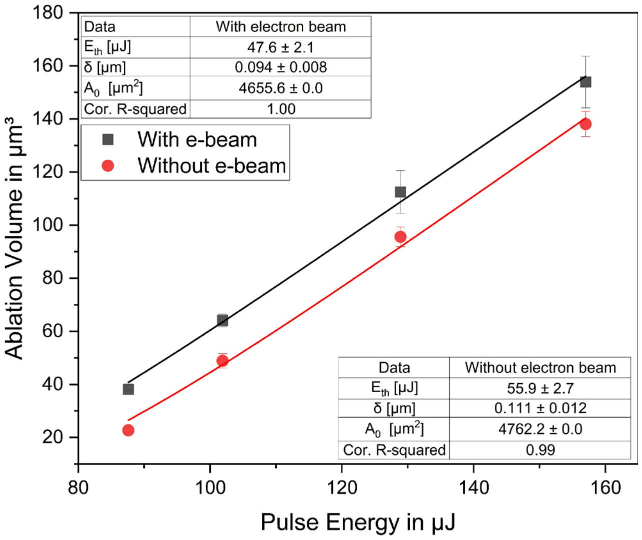

Fig. 5 Ablation crater volume plotted against the pulse energy without (red circles) and with (black squares) prior electron beam irradiation. The data was fitted using equation (7). E_{th} is the derived threshold energy, defined by the intersection of the fit-function and the x-axis.

In order to fit the data in Fig. 5 to equation (7), A_0 was taken from the previous area versus energy plot in Fig. 4. This resulted in the fit deviation value of zero for A_0. The threshold values with and without electron irradiation are 47.6 µJ and 55.9 µJ respectively indicating a decrease of 14.9 % due to the irradiation. Thus, the volume plot implies a stronger effect of the electron bombardment on the ablation threshold compared to the 3.8 % effect depicted by the area plot. This originates from the altered crater shape which deviates from the assumed paraboloid shape. Directly comparing the thresholds of the different evaluation methods ($E_{th,V}$ and $E_{th,A}$) makes this even clearer (see Table 2).

Table 2 Comparison between the threshold of the area and volume evaluation method for the two different experimental settings.

Threshold	Electron beam	Value in µJ	Threshold difference
$E_{th,V}$	On	47.6	24.4 %
$E_{th,A}$	On	63.0	
$E_{th,V}$	Off	55.9	14.8 %
$E_{th,A}$	Off	65.5	

The threshold difference between the methods is significantly more pronounced for the irradiated glass. Equation (7) was derived under the assumption of a paraboloidal crater shape ($V = ½ * h * A_0$) which seems incorrect due to these deviations. With regard to the crater profiles (see Fig. 3), it can also be seen that the crater shapes differ greatly, especially for higher pulse energies, which could be accounted by the non-gaussian profile resulting from the hard aperture in the beam path. For high energies the crater edges are steeper while the bottom flattens out. It is evident that the proposed relationship requires refinement. Furthermore, the relationship between A and V is likely to be functionally dependent on the pulse energy, thereby rendering the volume threshold questionable.

The deviation between the thresholds for electron beam irradiated specimens (24.4 %) is higher compared to the non-irradiated specimens (14.8 %). This finding is a consequence of the altered crater morphology by the injected electrons.

4. Conclusion

Femtosecond laser ablation experiments were conducted on soda-lime glass slides within the chamber of a scanning electron microscope. In order to analyze the influence of electron beam irradiation on the ablation threshold, the experiments were repeated with electron injection of the specimen via the SEM electron gun. The ablation crater height profiles were captured with a laser scanning microscope and the crater surface areas as well as the crater volumes determined. The area and volume data was subsequently fitted by modified threshold equations for the extraction of the volume- and area-dependent ablation threshold energies $E_{th,V}$ and $E_{th,A}$. It was shown, that prior electron irradiation can significantly reduce the ablation threshold of soda-lime glasses but additionally depends on the evaluation method ($\Delta E_{th,V} = 14.9$ % and $E_{th,A} = 3.8$ %).

In the case of ideally paraboloid shaped craters, $E_{th,V}$ and $E_{th,A}$ should be identical. It is evident that the threshold definition proposed by Liu, particularly in the context of the modified volume form, is not applicable for the evaluation of electron-irradiated samples without further consideration. In this regard, there is a need for the development of more sophisticated models that take into account the dependence of crater shape, especially if the craters are altered by extrinsic factors like electron beam irradiation.

Nonetheless, the findings demonstrate that extrinsic electrons have the potential to be utilized to seed the ablation in specific localized areas, by lowering the ablation threshold. Thus, with a subsequent laser pulse below the materials initial ablation threshold ablation would solely occur in the preirradiated areas. Since modern SEMs can achieve a resolution of less than 10 nm, further experiments should be carried out to determine whether laser ablation can be triggered solely by localized electron irradiation with a resolution beyond the laser diffraction limit.

Acknowledgements

The authors would like to express their sincere gratitude for the support provided by the Graduate School in Advanced Optical Technologies (SAOT) at the Friedrich-Alexander University of Erlangen-Nürnberg. This work was funded by the Deutsche Forschungsgemeinschaft (DFG), Grant Number: 504166000

References

[1] T.H. Maiman: Nature, 187, (1960) 493.
[2] A. Javan, W.R. Bennett, and D.R. Herriott: Phys. Rev. Lett., 6, (1961) 106.
[3] A.J. DeMaria, W.H. Glenn, M.J. Brienza, and M.E. Mack: Proc. IEEE Conf. Laser Eng. Appl., (1969) 2.
[4] R.L. Fork, B.I. Greene, and C.V. Shank: Appl. Phys. Lett., 38, (1981) 671.
[5] D. Tan, K.N. Sharafudeen, Y. Yue, and J. Qiu: Prog. Mater. Sci., 76, (2016) 154.

[6] J. Fourkas "Multiphoton lithography, processing and fabrication of photonic structures" ed. by A.D. Vainos, (Woodhead, Cambridge, 2012) p.139.
[7] D. Drouin, A.R. Couture, D. Joly, X. Tastet, V. Aimez, and R. Gauvin: Scanning, 29, (2007) 92.
[8] J.M. Liu: Opt. Lett., 7, (1982) 196.
[9] R. Halíř and J. Flusser: Proc. 6th Int. Conf. Central Europe Comput. Graph. Vis., (1998) 125.
[10] A. Andrásik, J. Budai, T. Szörényi, C. Vass, R. Flender, and B. Hopp: Appl. Phys. A, 129, (2023) 515.
[11] A. Ben-Yakar, A. Harkin, J. Ashmore, R.L. Byer, and H.A. Stone: J. Phys. D Appl. Phys., 40, (2007) 1447.
[12] M.I. Ojovan: Adv. Condens. Matter Phys., 2008, (2008) 817829.
[13] I. Mirza, N.M. Bulgakova, J. Tomáštík, V. Michálek, O. Haderka, L. Fekete, and T. Mocek: Sci. Rep., 6, (2016) 39133.
[14] P.S. Sneftrup, J.L. Hansen, S.G. Balslev, and P. Balling: Appl. Phys. A, 130, (2024) 646.
[15] D. Nieto, J. Arines, G.M. O'Connor, and M.T. Flores-Arias: Appl. Opt., 54, (2015) 8596.
[16] A. Ben-Yakar and R.L. Byer: J. Appl. Phys., 96, (2004) 5316.
[17] E. Stathatos, G.C. Vosniakos, and D. Pantelis: Solid State Phenom., 261, (2017) 129.
[18] A. Žemaitis, M. Gaidys, P. Gečys, and M. Gedvilas: Sci. Rep., 14, (2024) 5614.

(Received: June 24, 2025, Accepted: September 28, 2025)